Search for Infrasound Signals in InSight Data Using Coupled Pressure/Ground Deformation Methods

Raphael Garcia, Naomi Murdoch, Ralph Lorenz, Aymeric Spiga, Daniel Bowman, Philippe Lognonné, Don Banfield, William Bruce Banerdt

Search for infrasound signals in InSight data using coupled pressure/ground deformation methods

Raphael F. Garcia[1], Naomi Murdoch[1], Ralph Lorenz[2], Aymeric Spiga[3,4], Daniel C. Bowman[5], Philippe Lognonné[6], Don Banfield[7], William Bruce Banerdt[8]

[1]Institut Supérieur de l'Aéronautique et de l'Espace (ISAE-SUPAERO), Université de Toulouse, 10 Ave E. Belin 31400 Toulouse, France
[2]Applied Physics Laboratory, 11100 Johns Hopkins Road, Laurel, Maryland 20723, USA
[3]Laboratoire de Météorologie Dynamique / Institut Pierre-Simon Laplace (LMD/IPSL), Sorbonne Université, Centre National de la Recherche Scientifique (CNRS), École Polytechnique, École Normale Supérieure (ENS), 4 place Jussieu 75005 Paris, France
[4]Institut Universitaire de France (IUF), 1 rue Descartes, 75231 PARIS CEDEX 05, France
[5]Sandia National Laboratories, Albuquerque, NM 87023, USA
[6]Université de Paris, Institut de physique du globe de Paris, CNRS, F-75005 Paris, France
[7]Cornell Center for Astrophysics and Planetary Science, Cornell University, Ithaca, NY, 14853, USA
[8]Jet Propulsion Laboratory, California Institute of Technology, Pasadena, CA 91109, USA

Declaration of Competing Interests

The authors acknowledge there are no conflicts of interest recorded.

Key Points:

- An infrasound discriminator is defined and applied to 1.5 years of InSight pressure and seismic data.
- Horizontally propagating infrasound from local sources is rarely seen by both pressure and seismic instruments.
- Acoustic signals from Martian convective vortices are not detected by both pressure and seismic instruments.

Corresponding author: Raphael F. Garcia, raphael.garcia@isae.fr

Abstract

The unprecedented quality and sampling rate of seismometer and pressure sensors of InSight Mars mission allow us to investigate infrasound through its pressure and ground deformation signals. This study focus on compliance effects induced by acoustic waves propagating almost horizontally close to the surface. The compliance of acoustic waves is first estimated by using the compliance estimates from pressure perturbations moving at wind speed. Then, a marker of compliance events is used to detect events of ground deformation induced by pressure variations, in 3 frequency bands from 0.4 to 3.2 Hz, from Insight sol 180 to 690. Additional selection criteria are imposed on the detected events in order to focus on acoustic waves, and to remove various noise sources (e.g. wind effects or seismometer artefacts). After an automated selection, the visual inspection of the records allows us to validate two infrasound candidates that cannot be related to pressure perturbations moving at wind speed nor to known noise sources. For our highest quality infrasound candidate, the relation between this event and a convective vortex occuring 10 seconds later is tested. The azimuth of the vortex position at the time of infrasound detection is not consistent with the arrival azimuth of the suspected infrasound inferred from the polarization of seismometer records, thus the link between these two phenomena cannot be demonstrated. Further investigations would require a better understanding of wind-related noise impacting InSight sensors, and of the effects of lateral variations of sub-surface mechanical properties on the ground deformations induced by atmospheric pressure variations.

1 Introduction

Forces imposed on planetary atmospheres can generate low frequency acoustic wave that may travel long distances. The monitoring of infrasound signals in Earth's atmosphere has many applications (Le Pichon et al., 2010). Likewise, sound-generating phenomena on Mars could include bolide airbursts and impacts, spacecraft entry, seismic activity, landslides, wind-mountain interactions, atmospheric turbulence, and convective vortices. However, the particular conditions of Mars' atmosphere do not favour their observation due to the stronger attenuation by carbon dioxide (Bass & Chambers, 2001; Williams, 2001). In addition, strong temperature inversions allowing long distance acoustic transmission exist only close to the surface during the night (Garcia et al., 2017; Martire et al., 2020).

Infrasound observations on other planets have become possible only recently with InSight NASA Discovery mission (Banfield et al., 2020; Martire et al., 2020). The InSight mission landed on Mars' surface on 26 November 2018 at sol (martian day) zero of the mission (Banerdt et al., 2020). The robotic arm deployed the seismometer SEIS (Seismic Experiment for Interior Structure) (Lognonné et al., 2019) and its wind and thermal shield. A full suite of meteorological sensors operates on the lander, including a pressure sensor, wind sensors and air temperature sensors (Banfield et al., 2019). The SEIS sensors record seismic signals (Giardini et al., 2020), which can be used to infer the structure of the near-surface (Lognonné et al., 2020) and deep interior. In addition, the meteorological sensors reveal atmospheric dynamics with unprecedented precision (Banfield et al., 2020).

The SEIS data are dominated by ground motions induced by atmospheric activity and these signals have been used to infer both the atmosphere dynamics (Garcia, Kenda, et al., 2020; Murdoch et al., 2021; Charalambous et al., 2021) and the elastic properties of the sub-surface (Kenda et al., 2020).

After an initial assessment of potential infrasound in InSight's pressure data set (Banfield et al., 2020), it was quickly recognized that ground deformations must be combined with the pressure records in order to ascribe a given pressure perturbation to an infrasound phenomenon. The usual terrestrial infrasound detection methods

exploit a distributed network of sensors to extract the propagation direction and apparent velocity, and to confirm the acoustic character of the signal. In the absence of such instrumentation, we must use the ground deformations to reach the same goals. Martire et al. (2020) described in detail how infrasonic waves generate ground deformations by direct conversion to seismic waves or by static ground deformations through compliance effects (Sorrells et al., 1971), which are further described below. These authors even suggested that some events detected by SEIS may be compliance effects induced by infrasound of an amplitude too small for a detection by the pressure sensor. These detections occurred at night when atmospheric conditions were favorable for long-distance acoustic transmission. Stutzmann et al. (2021) also provided, among other hypotheses, a model of infrasound production and propagation in order to explain elliptically polarized signals observed in SEIS records. This study also demonstrates that, around 1 Hz, ground deformations recorded by SEIS have a signal to noise ratio about 30 times larger than pressure records for infrasound forcing. However, no infrasound signals have been observed simultaneously on both pressure and SEIS sensors, so far.

The present study proposes an extensive exploration of the InSight SEIS, pressure and wind data sets in order to search for infrasound signals that produce ground deformations through compliance effects. Such signals must propagate nearly horizontally to create this effect, a case that occurs only when either a low altitude waveguide is present or the acoustic source is very close to the sensor. As demonstrated by Martire et al. (2020), the nocturnal temperature inversion and wind jet present favorable conditions for long distance, nearly horizontal infrasound propagation. Such conditions are much rarer during the day, relying on a very strong low-altitude wind to refract sound back towards the surface of the planet at a shallow enough angle to induce compliance effects. Alternatively, an acoustic event close enough to the sensor for direct (non refracted) sound propagation could be captured via compliance. On Earth, the general rule is that these signals are attenuated at or slightly faster than spherical geometric spreading would suggest - a value of r^{-1} to $r^{-1.1}$, where r denotes range, has been reported (Bowman, 2019; Institute, 1983). The low-level temperature and wind structure can greatly enhance or attenuate the signals, depending on the specific regime (Wilson et al., 2015).

The next section describes how vertical compliance is estimated for acoustic waves by using estimates from common pressure perturbations. Then, the data set and processing methods are described. A section is dedicated to additional selection criteria that are imposed to exclude signals generated by wind, meteorological pressure perturbations and SEIS artifacts. The detection results are presented in a dedicated section. These results are then discussed to in terms of infrasound sources and propagation conditions. The consistency between infrasound emitted by a convective vortex and the measured signals is tested for one particular example. Finally, we conclude on the interest of such infrasound sensing and future directions.

2 Ground compliance for infrasounds and design of a specific marker

The ground movements of the Mars surface induced by atmospheric pressure perturbations have been described and analyzed by Kenda et al. (2020), whereas Martire et al. (2020) considered specifically the effect of infrasound. The theoretical background for the ground response to an horizontally propagating plane pressure wave pressure is provided by Sorrells et al. (1971) for an homogeneous half-space and by Kenda et al. (2017); Tanimoto and Wang (2019) for a layered ground structure. These theoretical results predict that inertial compliance effects dominate around 1 Hz for acoustic waves due to their large propagating speed (about 250 m/s in Mars' atmosphere). In addition, horizontal ground velocity along the plane wave propagation direction is in phase with pressure, whereas vertical ground velocity is phase shifted

by 90° relative to Pressure. For layered media, the vertical compliance relation can be written Kenda et al. (2017):

$$V^Z(f) = -icC_N^Z(\lambda_h)P(f) \tag{1}$$

in which f is the frequency of the pressure wave, λ_h its horizontal wavelength, c its horizontal propagation speed, P the atmospheric pressure, V^Z the vertical ground velocity, C_N^Z the normalized vertical compliance (vertical compliance divided by the horizontal velocity of the pressure signal) and i the purely imaginary complex number. An interesting property of this formula is that the normalized vertical compliance depends only on the horizontal wavelength of the pressure wave, meaning that even for a complex stratified media, the amount of ground response along the vertical depends only on the horizontal wavelength of the pressure forcing (λ_h) and its horizontal propagation speed (c). Because C_N^Z has been estimated by Kenda et al. (2020) for pressure perturbations moving at wind speeds in the 0.04-0.8 Hz frequency range, knowing the sound speed c and using an average wind speed of 5 m/s, the equation 1 allows us to estimate the vertical compliance of acoustic waves of the same horizontal wavelengths in the 2-20 Hz frequency range. To do so, we note the following relation between frequency, horizontal wavelength and the speed of horizontal propagation of the pressure wave: $\lambda_h = \frac{c_s}{f_s} = \frac{c_w}{f_w}$, where c_s and f_s are the speed and frequency of a sound wave, and c_w and f_w are the wind speed and frequency of an atmospheric pressure perturbation moving with the wind. Thus the normalized vertical compliance estimated as a function of frequency in Kenda et al. (2020) $C_N^Z(f_w)$ can be converted to the one of acoustic waves by using the relation relating the frequencies and propagation speeds at constant wavelength: $f_w = \frac{c_w}{c_s} f_s$. Because the ratio $\frac{c_w}{c_s}$ is about 1/50 (for a wind speed of 5 m/s), it allows recovery of the vertical normalized compliance for acoustic frequencies 50 times larger than the range previously investigated (Kenda et al., 2020). Figure 1 presents the normalized vertical compliance C_N^Z as a function of frequency estimated in Kenda et al. (2020), and its conversion into vertical compliance ($\frac{V^Z}{P}$) for acoustic waves. The values obtained are extrapolated to frequencies down to 0.4 Hz by using a power law ($\frac{V^Z}{P} = (6E-7) * f^{0.6}$). With these assumptions, we obtain an estimate of vertical compliance of acoustic waves relying on real measurements of atmospheric pressure perturbations. At the same frequency, the vertical compliance values obtained for acoustic waves are a factor 10 larger than the ones measured on atmospheric pressure perturbations. As a consequence, in order to detect infrasounds, we re-use the compliance marker defined by Kenda et al. (2020), and select in each frequency range only the compliance events with measured vertical compliance close to the estimated one. These events are considered as potential detections of acoustic waves.

3 Data set and processing

This study uses data of SEIS VBB VEL channel at 20 samples par seconds from sol 185 to sol 680 (InSight Mars SEIS Data Service, 2019). The raw VBB data are corrected for "tick noise" (Compaire et al., 2021), and for glitch effects (Scholz et al., 2020). After removing the transfer function of SEIS-VBB-VEL components, the ground velocity is estimated along vertical, North and East directions. The calibrated air pressure, wind speed and direction are obtained from APSS pressure and wind sensors (Banfield et al., 2019).

The ground velocity and atmospheric pressure channels are band-pass filtered in various frequency bands from 0.05 Hz to 3.2 Hz (Kenda et al., 2020). However, for infrasound monitoring, we focus on the three bands around 1 Hz: 0.4-0.8 Hz, 0.8-1.6 Hz and 1.6-3.2 Hz. In each frequency band, the compliance marker defined in Kenda et al. (2020) is computed at all times by using pressure data (P), vertical ground velocity (V_z) and horizontal ground velocity along the East direction (V_h). The East component

is chosen because it is known to be more sensitive to compliance effects than North component (Garcia, Kenda, et al., 2020). We recall here the formula of the compliance marker (Kenda et al., 2020):

$$\mathrm{I_G}(t) = \frac{STA(P^2)}{LTA(P^2)} CC_T(P, \mathrm{Hil}(V_z)) CC_T(P, V_h) CC_T(\mathrm{Hil}(V_z), V_h) \tag{2}$$

where $\mathrm{Hil}(V_z)$ is the Hilbert transform of vertical velocity record, the $STA()$ and $LTA()$ functions stand respectively for Short Term Average performed on the time interval $[t - T/2, t + T/2]$, and Long Term Average performed on $[t - 20T/2, t + 20T/2]$, and the $CC_T(X, Y)$ function stands for Correlation Coefficient between X and Y for the time range $[t - T/2, t + T/2]$. T is defined by $T = \frac{3}{f_1}$, with f_1 being the lower bound of the frequency range considered. The last three terms of the equation should be equal to one if in the time range $[t - T/2, t + T/2]$, P, $\mathrm{Hil}(V_z)$ and V_h are perfectly correlated, as expected from compliance relation. The first term is an amplitude ratio ensuring that the pressure variations are above background noise.

Compliance events are defined when the value of this marker is above 0.3, corresponding to average correlation coefficients above 0.7. For the three frequency bands of interest ([0.4-0.8 Hz], [0.8-1.6 Hz], [1.6-3.2 Hz]) a total of 15995 compliance events are detected. A bivariate histogram of the vertical compliance values obtained by this process is presented in Figure 2.(a) as a function of the frequency band. Almost all these values are due to atmospheric pressure perturbations moving at wind speed. In order to search for infrasound signals among all compliance events, we will keep only events with a vertical compliance within -50% and +300% of the estimated acoustic compliance value (within black dashed lines in figure 2.(a)). In accordance with compliance theory for acoustic waves in this frequency range, where tilt effects can be neglected, we also require that the energy along the vertical component is larger than along the East component during the event (Kenda et al., 2020; Martire et al., 2020). Finally, we impose the constraint of STA/LTA values above 1.5 for pressure, and 2 for vertical ground velocity, in order to ensure a high enough signal to noise ratio of these signals on the two instruments. After these selections steps, a total of 3989 compliance events are kept for analysis over the three frequency bands.

In order to validate our infrasound marker approach, we present an application on an Earth data set acquired during the quarry blast experiments by Garcia, Martire, et al. (2020). During this experiment, collocated infrasound and seismometer instruments, 190 m from away the source, recorded the fall of a cliff (20x20x40 m) following a quarry blast of a total of 900 kg of TNT. This event generated a strong acoustic wave with a 10-20 Pa amplitude and a period around 1 Hz. These data are filtered in the 0.8-1.6 Hz frequency band. The infrasound markers are computed with the same process applied to Mars data. Figure 3 shows the raw and filtered data, as well as the infrasound marker for this event. As expected for compliance effects, the East ground velocity component, pointing in direction of the source, is in phase with the pressure signal, whereas the vertical ground velocity is shifted by 90° relative to these two signals. As a consequence, the product of correlation coefficients in equation (2) increase to 0.4, and the infrasound marker $\mathrm{I_G}(t)$ has a maximum value of 8 due to the large signal to noise of the pressure signal. However, the horizontal ground velocity signal is larger than the vertical , whereas compliance theory (Sorrells et al., 1971) predicts it should be smaller. This discrepancy is probably due to movements of the base plate on which the seismometer was installed, or to a direct action of the acoustic wave on the seismometer surface because the sensor was not buried. Despite this discrepancy on the amplitude of the seismometer signals, this example demonstrates the efficiency of the infrasound marker approach on a terrestrial data set. Other examples of compliance effects generated by terrestrial infrasound are also available in the study by McKee et al. (2018).

4 Potential contaminations by other signals

Both Pressure and SEIS sensors are subject to various noise sources that can mimic the expected infrasound signals, we describe here the three main origins of these signals that can be falsely interpreted as infrasonic signals, and how these are mitigated.

4.1 Wind effects

The main noise source that can contaminate our analysis is due to wind effects on the lander and on the pressure sensor. As described by Lognonné et al. (2020), the ground velocity measurements in the 0.4-1.5 Hz range have an energy that increases with wind strength. This wind dependency is probably mainly due to lander vibrations under the wind (Murdoch et al., 2016). This environment noise is mainly polarized along the wind direction (Charalambous et al., 2021). The pressure sensor is also affected by wind noise. Charalambous et al. (2021) demonstrated that during day time there is an almost linear relation between the energies of pressure and vertical ground velocity. By using figure 3 of Charalambous et al. (2021), we can estimate an apparent compliance value as a function of frequency for this relation. This estimate provides compliance values almost identical to the estimated acoustic compliance. As a consequence, we cannot use the compliance as a criteria to discriminate between infrasound and wind effects. However, figure 4 shows that during day time the background noise produces coherent signals between vertical and East component of ground velocity, with a phase close 170° in the 0.4-3.2 Hz range. This phase relation is consistently observed in the 0.4-3.2 Hz range over the sol range considered here (185-690), and the average phase remains in the 165°-195° range. In order to exclude this noise dominated by wind effects, we add to our selection criteria $|CC_T(\mathrm{Hil}(V_z), V_h)| > 0.9$ which is ensuring that the phase relation between vertical and East SEIS component is close to 90°, as expected for acoustic compliance events. In addition, during the manual review of potential infrasound events, we also track the excitation of the 4 Hz resonance observed in vertical ground velocity measurements. This resonance is ascribed to lander vibrations under wind drag (Giardini et al., 2020; Ceylan et al., 2021), and it is a good marker of both wind speed and wind contamination of SEIS records.

4.2 Effect of atmospheric pressure perturbations

Atmospheric pressure perturbations moving with the wind also induces compliance effects. Because the compliance depends linearly on the wind speed, for high wind speeds and soft soils these perturbations can have large compliance values. In order to decipher unambiguously between infrasounds and the atmospheric pressure perturbations, we compute the measured compliance normalized to wind speed for all observations. The obtained values must be close to the estimated acoustic compliance divided by 6 m/s (red line in figure 2.(b)), and in any case must appear as outlayers relative to the values obtained for usual atmospheric pressure perturbations (background color in figure 2.(b)).

4.3 Donks, glitches and their high frequency precursor in SEIS records

The SEIS data suffer from various artifacts that have been described by Ceylan et al. (2021). The "donks" are burst of high frequency energy, probably associated with thermal cracks. These signals can occur several times during a minute, and their temporal distribution evolves with the temperature of the atmosphere (Compaire et al., 2021). However, these signals are usually restricted to frequencies above 10 Hz, and their impact below 3.2 Hz (maximum frequency considered in this study) can be considered as negligible.

As described by Scholz et al. (2020), SEIS data are contaminated by glitches of different origins that are sometimes initiated by a high frequency precursor that may impact our frequency range. Such signals can, by chance, present the proper SEIS and pressure phase relations. When it happens, due to their large amplitude on SEIS components, such events will be selected due to their large apparent compliance. Only a visual inspection of raw VBB waveforms allows detection of such contamination by glitches. Thus, this inspection is performed during the manual review of selected events.

5 Results

The compliance detection method presented in Kenda et al. (2020) is applied to the sol range 183-690 resulting in the detection of 15995 compliance events in the three frequency bands. The selection method presented in section 3 reduced this number to 3989 events. The additional constraints set to mitigate wind and pressure perturbation effects described in section 4 further reduces this number to 95 events. Most of these events are during the turbulent period of the day and within 15 seconds to a pressure drop induced by a convective vortex. Then, these events are revised manually in order to:

- ensure that the maximum of the marker corresponds to the main signal and update accordingly the compliance, wind and other parameters in case of time shifts (always smaller than 10 seconds)
- reject glitch events by reviewing raw VBB waveforms
- reject events corresponding to an increase of wind speed to avoid wind effects
- reject events for which an excitation of the 4 Hz resonance is observed on vertical ground velocity at the same time than the potential infrasound

Among these 95 events, about one third are rejected due to glitch signals, one third due to suspected wind contamination, and one third due to too low normalized compliance. After this manual inspection only 2 events remain as solid candidates for infrasounds. The compliance and normalized compliance values of these events are presented as red circles in figure 2.

A similar analysis was performed in 4 frequency bands covering the 0.025-0.4 Hz frequency range. In this frequency range, the infrasound compliance estimate is quite uncertain, but we still expect inertial compliance effects to dominate tilt effects, and so a vertical to horizontal ground velocity amplitude ratio larger than 1. No infrasound candidates have been detected in this frequency range.

The waveforms of the two infrasound candidate events are shown in figure 5. These two events occur during the day time, a few tens of seconds before a pressure drop. These suspected infrasound signals present high signal to noise ratio on both Pressure and SEIS records, and the proper phase relation between SEIS components and pressure. The SEIS signals are followed by other signals for which the vertical and East components are almost in phase opposition and simultaneous to an increase in wind speed, as expected for wind effects described in section 4.1. For these events, the SEIS vertical to horizontal ratio is around 4, a bit larger than predicted by compliance theory, but it can be explained by the projection of only a part of the ground movements along the East direction.

6 Discussion

Our detection method extracts two events for which high signal to noise ratio signals are observed simultaneously on Pressure and SEIS records, and with the proper

phase and amplitude relations expected for infrasound compliance effects. These signals cannot be due to wind and glitch noise sources and present normalized compliance values significantly larger than usual pressure perturbations moving at wind speed. These events occur during the turbulent period of the atmosphere, and are close to pressure drop signals (see Spiga et al. (2021) for an extensive analysis of day time convective vortices observed by InSight). Vortices responsible for these pressure drops have been suggested as potential sources for infrasound signals (Bedard, 2005).

6.1 Can these infrasounds be generated by convective vortices?

In order to test the hypothesis of infrasounds generated by convective vortices, the track of the vortices has been estimated following the method described in Murdoch et al. (2021). This process is presented for the potential infrasound event on sol 521. The pressure drops associated to other candidate on sol 421 are too small to ensure a signal to noise high enough for a proper estimate of the convective vortex trajectory. Figures 6.(a) to 6.(d) present the data fit and the reconstructed trajectory close to dust devil closest distance. The propagation direction of the best fit model is consistent with a local wind direction measured by the TWINS (Temperature and Wind for InSight) wind sensors around 20° azimuth. The azimuth of the vortex at the time of infrasound detection (neglecting sound propagation time) is estimated to be around 45° (black square in figure 6.(d)). Figures 6.(e) and 6.(f) provide the polarization of SEIS records, filtered in the 0.8-1.6 Hz band, during the event. The dominant azimuth in the horizontal plane is about 80°±30° with a 180° ambiguity. The counter-clockwise rotation in the vertical plane seen from South allows us to remove this ambiguity by using compliance theory (Sorrells et al., 1971; Martire et al., 2020), thus pointing a pressure wave coming from 260°±30° azimuth. The significant discrepancy between these two directions suggests that the suspected signals cannot be produced by this convective vortex. Our data set is limited to localized measurements, it does not recover the full complexity the atmosphere dynamics during day time turbulent period. As a consequence, we cannot completely exclude that such signals have been generated by more distant atmospheric sources.

6.2 Additional complexities

Despite our conservative selection criteria trying to avoid wind contamination effects of SEIS records, these effects are not yet fully understood. In particular, changes of wind orientation over short periods of time may generate complex SEIS signals. A full model of interaction between InSight system elements and wind is required too ensure a proper identification of these wind related signals in SEIS data.

Another element of complexity is the lateral variations of sub-surface properties inside the hollow crater in which InSight landed. These variations are suspected to be at the origin of the asymmetric distribution of convective vortices detected by InSight (Murdoch et al., 2021), and to the slightly larger compliance values observed along East direction than along the North direction (Garcia, Kenda, et al., 2020). The sub-surface at the center of the hollow crater is softer than outside the crater. To properly model the ground response to pressure forcing would require a full 3D model.

Finally, both pressure and wind sensors present noise levels that are higher than the theoretical sensitivity of SEIS-VBB sensors to compliance effects in the frequency range considered here (0.4-3.2 Hz) (Stutzmann et al., 2021).

7 Conclusion

Our study presents a method to detect compliance events generated by acoustic waves. This method relies on phase relations between Pressure and SEIS records, as

well as observed vertical compliance for high signal to noise ratio signals. A strict selection of compliance events is performed in order to exclude all potential contamination by wind, meteorological pressure perturbations, and SEIS artefacts. After this selection, only two events, among more than 3000 potential acoustic compliance events, are selected and discussed. The consistency between the geometry and characteristics of the convective vortex and the propagation direction of the detected infrasound estimated from SEIS polarization is checked for one particular event. Based on this analysis, the suspected infrasound signals cannot be convincingly linked to the convective vortex that is detected ten seconds later. If the signals are truly from infrasound, they were either transmitted from some distance away via a duct formed by a low-altitude wind jet, or they were generated quite close – likely less than a few tens of kilometers from the lander.

Even if we try to overcome the intrinsic difficulty of having a single pressure sensor and seismometer located at approximately the same position by using ground deformation records, the extensive exploration of the InSight data base provides only two high signal to noise infrasound candidates that can hardly be explained by known noise sources. In order to go beyond this first analysis, both a better understanding of wind-related noise and a better modeling of ground response using 3D sub-surface models are required.

Data and Resources

InSight's SEIS data are available at IRIS-DMC and PDS in SEED format. SEIS data are referenced at http://dx.doi.org/10.18715/SEIS.INSIGHT.XB_2016. InSight's APSS data are archived at the Planetary Data System Atmospheres node (`https://atmos.nmsu.edu/data_and_services/atmospheres_data/INSIGHT/insight.html`). The terrestrial data set shown in Figure 3 is available here: `https://doi.org/10.5281/zenodo.4067121`.

Acknowledgments
The authors acknowledge there are no conflicts of interest recorded. This study is InSight contribution number 196. The French authors acknowledge the French Space Agency CNES and ANR (ANR-14-CE36-0012-02 and ANR-19-CE31-0008-08) for funding the InSight Science analysis. D. Bowman acknowledges funding from the NASA Solar System Workings program (19-SSW19-0042). Sandia National Laboratories is a multimission laboratory managed and operated by National Technology & Engineering Solutions of Sandia, LLC, a wholly owned subsidiary of Honeywell International Inc., for the U.S. Department of Energy's National Nuclear Security Administration under contract DE-NA0003525. This paper describes objective technical results and analysis. Any subjective views or opinions that might be expressed in the paper do not necessarily represent the views of the U.S. Department of Energy or the United States Government. We acknowledge NASA, CNES, their partner agencies and Institutions (UKSA, SSO, DLR, JPL, IPGP-CNRS, ETHZ, IC, MPS-MPG) and the flight operations team at JPL, SISMOC, MSDS, IRIS-DMC and PDS for providing SEED SEIS data. SEIS data are referenced at http://dx.doi.org/10.18715/SEIS.INSIGHT.XB_2016. InSight's APSS data are archived at the Planetary Data System Atmospheres node (`https://atmos.nmsu.edu/data_and_services/atmospheres_data/INSIGHT/insight.html`).

References

Banerdt, W. B., Smrekar, S. E., Banfield, D. J., Giardini, D., Golombek, M. P., Johnson, C. L., ... Wieczorek, M. A. (2020, 2). Initial Results from

the InSight Mission on Mars. *Nature Geoscience*. Retrieved from http://www.nature.com/articles/s41561-020-0544-y doi: 10.1038/s41561-020-0544-y

Banfield, D. J., Rodriguez-Manfredi, J. A., Russell, C. T., Rowe, K. M., Leneman, D., Lai, H. R., ... Banerdt, W. B. (2019, 2). InSight Auxiliary Payload Sensor Suite (APSS). *Space Science Reviews*, *215*(1), 4. Retrieved from http://link.springer.com/10.1007/s11214-018-0570-x doi: 10.1007/s11214-018-0570-x

Banfield, D. J., Spiga, A., Newman, C. E., Forget, F., Lemmon, M. T., Lorenz, R. D., ... Banerdt, W. B. (2020, 2). The atmosphere of Mars as observed by InSight. *Nature Geoscience*. Retrieved from http://www.nature.com/articles/s41561-020-0534-0 doi: 10.1038/s41561-020-0534-0

Bass, H. E., & Chambers, J. P. (2001). Absorption of sound in the Martian atmosphere. *The Journal of the Acoustical Society of America*, *109*(6), 3069–3071. Retrieved from http://asa.scitation.org/doi/10.1121/1.1365424 doi: 10.1121/1.1365424

Bedard, A. J. (2005). Low-frequency atmospheric acoustic energy associated with vortices produced by thunderstorms. *Monthly Weather Review*, *133*(1), 241–263. doi: 10.1175/MWR-2851.1

Bowman, D. C. (2019). Yield and emplacement depth effects on acoustic signals from buried explosions in hard rock. *Bulletin of the Seismological Society of America*. doi: 10.1785/0120180285

Ceylan, S., Clinton, J. F., Giardini, D., Böse, M., Charalambous, C., van Driel, M., ... Perrin, C. (2021, January). Companion guide to the marsquake catalog from InSight, sols 0–478: Data content and non-seismic events. *Physics of the Earth and Planetary Interiors*, *310*, 106597. Retrieved from https://doi.org/10.1016/j.pepi.2020.106597 doi: 10.1016/j.pepi.2020.106597

Charalambous, C., Stott, A. E., Pike, W. T., McClean, J. B., Warren, T., Spiga, A., ... Banerdt, W. B. (2021, February). A comodulation analysis of atmospheric energy injection into the ground motion at InSight, mars. *Journal of Geophysical Research: Planets*. Retrieved from https://doi.org/10.1029/2020je006538 doi: 10.1029/2020je006538

Compaire, N., Margerin, L., Garcia, R., Pinot, B., Calvet, M., Orhand-Mainsant, G., ... Banerdt, W. B. (2021, March). Autocorrelation of the ground vibrations recorded by the SEIS-InSight seismometer on mars. *Journal of Geophysical Research: Planets*. Retrieved from https://doi.org/10.1029/2020je006498 doi: 10.1029/2020je006498

Garcia, R. F., Brissaud, Q., Rolland, L. M., Martin, R., Komatitsch, D., Spiga, A., ... Banerdt, W. B. (2017, 10). Finite-Difference Modeling of Acoustic and Gravity Wave Propagation in Mars Atmosphere: Application to Infrasounds Emitted by Meteor Impacts. *Space Science Reviews*, *211*(1-4), 547–570. doi: 10.1007/s11214-016-0324-6

Garcia, R. F., Kenda, B., Kawamura, T., Spiga, A., Murdoch, N., Lognonné, P. H., ... Banerdt, W. B. (2020). Pressure Effects on the SEIS-InSight Instrument, Improvement of Seismic Records, and Characterization of Long Period Atmospheric Waves From Ground Displacements. *Journal of Geophysical Research: Planets*, e2019JE006278. doi: 10.1029/2019JE006278

Garcia, R. F., Martire, L., Chaigneau, Y., Cadu, A., Mimoun, D., Portus, M. B., ... Martin, R. (2020, December). An active source seismo-acoustic experiment using tethered balloons to validate instrument concepts and modelling tools for atmospheric seismology. *Geophysical Journal International*. Retrieved from https://doi.org/10.1093/gji/ggaa589 doi: 10.1093/gji/ggaa589

Giardini, D., Lognonné, P. H., Banerdt, W. B., Pike, W. T., Christensen, U., Ceylan, S., ... Yana, C. (2020, 2). The seismicity of Mars. *Nature Geoscience*, *in press*. Retrieved from http://www.nature.com/articles/

s41561-020-0539-8 doi: 10.1038/s41561-020-0539-8

InSight Mars SEIS Data Service. (2019). *Seis raw data, insight mission.* IPGP, JPL, CNES, ETHZ, ICL, MPS, ISAE-Supaero, LPG, MFSC. doi: 10.18715/SEIS.INSIGHT.XB_2016

Institute, A. N. S. (1983). *Estimating air blast characteristics for single point explosions in air, with a guide to evaluation of atmospheric propagation and effects.* (ANSI S2.20-1983)

Kenda, B., Drilleau, M., Garcia, R. F., Kawamura, T., Murdoch, N., Compaire, N., ... Spohn, T. (2020, June). Subsurface structure at the InSight landing site from compliance measurements by seismic and meteorological experiments. *Journal of Geophysical Research: Planets*, *125*(6). Retrieved from https://doi.org/10.1029/2020je006387 doi: 10.1029/2020je006387

Kenda, B., Lognonné, P. H., Spiga, A., Kawamura, T., Kedar, S., Banerdt, W. B., ... Golombek, M. P. (2017). Modeling of Ground Deformation and Shallow Surface Waves Generated by Martian Dust Devils and Perspectives for Near-Surface Structure Inversion. *Space Science Reviews*, *211*(1-4), 501–524. Retrieved from http://dx.doi.org/10.1007/s11214-017-0378-0 doi: 10.1007/s11214-017-0378-0

Le Pichon, A., Blanc, E., & Hauchecorne, A. (2010). Infrasound monitoring for atmospheric studies. In *Infrasound monitoring for atmospheric studies* (1st ed., pp. 1–735). Dordrecht, Netherlands: Springer Dordrecht Heidelberg London New York. doi: 10.1007/978-1-4020-9508-5

Lognonné, P. H., Banerdt, W. B., Giardini, D., Pike, W. T., Christensen, U., Laudet, P., ... Wookey, J. (2019, 2). SEIS: Insight's Seismic Experiment for Internal Structure of Mars. *Space Science Reviews*, *215*(1), 12. Retrieved from http://link.springer.com/10.1007/s11214-018-0574-6 doi: 10.1007/s11214-018-0574-6

Lognonné, P. H., Banerdt, W. B., Pike, W. T., Giardini, D., Christensen, U., Garcia, R. F., ... U., C. (2020, 2). Constraints on the shallow elastic and anelastic structure of Mars from InSight seismic data. *Nature Geoscience*, *in press*(February). Retrieved from http://www.nature.com/articles/s41561-020-0536-y doi: 10.1038/s41561-020-0536-y

Martire, L., Garcia, R. F., Rolland, L. M., Spiga, A., Lognonné, P. H., Banfield, D. J., ... Martin, R. (2020). Martian Infrasound: Numerical Modeling and Analysis of InSight's Data. *Journal of Geophysical Research: Planets*. doi: XXXX

McKee, K., Fee, D., Haney, M. M., Matoza, R. S., & Lyons, J. (2018). Infrasound Signal Detection and Back Azimuth Estimation Using Ground-Coupled Airwaves on a Seismo-Acoustic Sensor Pair. *Journal of Geophysical Research: Solid Earth*, *123*(8), 6826–6844. doi: 10.1029/2017JB015132

Murdoch, N., Mimoun, D., Garcia, R. F., Rapin, W., Kawamura, T., Lognonné, P. H., ... Banerdt, W. B. (2016). Evaluating the Wind-Induced Mechanical Noise on the InSight Seismometers. *Space Science Reviews*. Retrieved from http://dx.doi.org/10.1007/s11214-016-0311-y doi: 10.1007/s11214-016-0311-y

Murdoch, N., Spiga, A., Lorenz, R., Garcia, R. F., Perrin, C., Widmer-Schnidrig, R., ... Banerdt, W. (2021, February). Constraining martian regolith and vortex parameters from combined seismic and meteorological measurements. *Journal of Geophysical Research: Planets*. Retrieved from https://doi.org/10.1029/2020je006410 doi: 10.1029/2020je006410

Scholz, J.-R., Widmer-Schnidrig, R., Davis, P., Lognonné, P., Pinot, B., Garcia, R. F., ... Banerdt, W. B. (2020, October). Detection, analysis, and removal of glitches from InSightś seismic data from mars. *Earth and Space Science*, *7*(11). Retrieved from https://doi.org/10.1029/2020ea001317 doi: 10.1029/2020ea001317

Sorrells, G. G., McDonald, J. A., Der, Z. A., & Herrin, E. T. (1971). Earth Motion Caused by Local Atmospheric Pressure Changes. *Geophysical Journal of the Royal Astronomical Society*, *26*(1-4), 83–98. doi: 10.1111/j.1365-246X.1971.tb03384.x

Spiga, A., Murdoch, N., Lorenz, R., Forget, F., Newman, C., Rodriguez, S., ... Banerdt, W. B. (2021, January). A study of daytime convective vortices and turbulence in the martian planetary boundary layer based on half-a-year of InSight atmospheric measurements and large-eddy simulations. *Journal of Geophysical Research: Planets*, *126*(1). Retrieved from `https://doi.org/10.1029/2020je006511` doi: 10.1029/2020je006511

Stutzmann, E., Schimmel, M., Lognonné, P., Horleston, A., Ceylan, S., van Driel, M., ... Spiga, A. (2021, January). The polarization of ambient noise on mars. *Journal of Geophysical Research: Planets*, *126*(1). Retrieved from `https://doi.org/10.1029/2020je006545` doi: 10.1029/2020je006545

Tanimoto, T., & Wang, J. (2019, June). Theory for deriving shallow elasticity structure from colocated seismic and pressure data. *Journal of Geophysical Research: Solid Earth*, *124*(6), 5811–5835. Retrieved from `https://doi.org/10.1029/2018jb017132` doi: 10.1029/2018jb017132

Williams, J.-P. (2001, 3). Acoustic environment of the Martian surface. *Journal of Geophysical Research: Planets*, *106*(E3), 5033–5041. Retrieved from `http://doi.wiley.com/10.1029/1999JE001174` doi: 10.1029/1999JE001174

Wilson, D. K., Pettit, C. L., & Ostashev, V. E. (2015). Sound propagation in the atmospheric boundary layer. *Acoustics Today*, *11*.

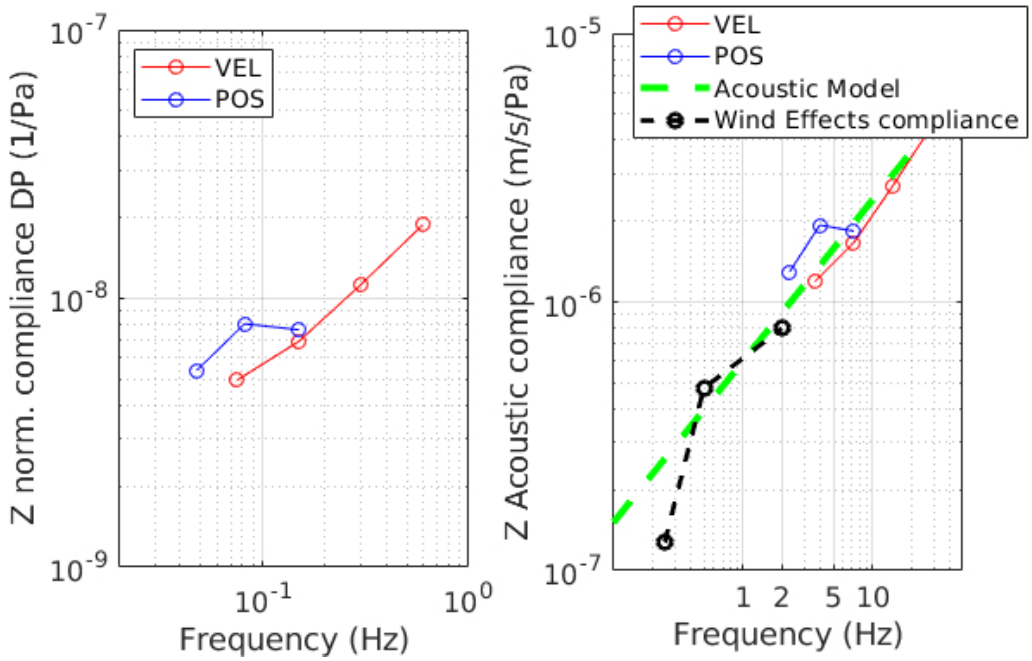

Figure 1. On the left, average normalized vertical compliance C_N^Z (in 1/Pa) obtained in Kenda et al. (2020) as a function of frequency (in Hz) from SEIS VBB VEL (in red) and POS (in blue) channels. On the right, vertical acoustic compliance (in m/(s*Pa)) estimated from C_N^Z values, power law model ($\frac{V^Z}{P} = (6E-7) * f^{0.6}$) extrapolating these values below 1 Hz (green dashed line), and apparent compliance due to wind effects (black dashed line) computed from figure 3 of Charalambous et al. (2021).

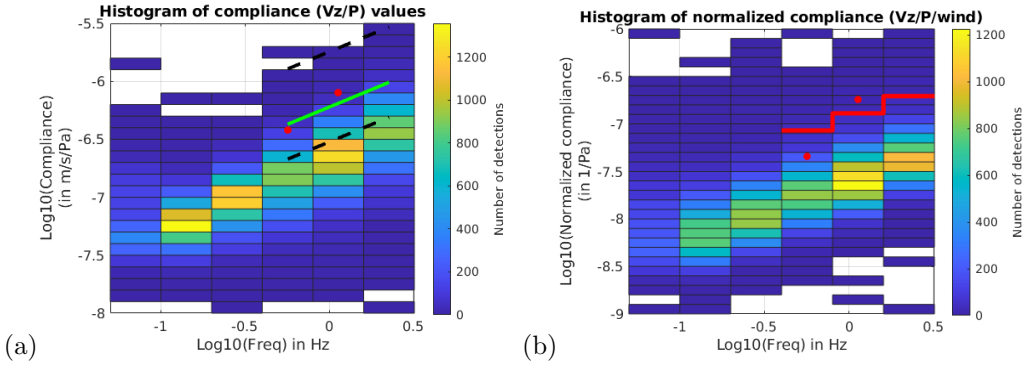

Figure 2. On the left, histogram of the number of compliance event detections (in color) as a function of logarithm of vertical compliance (in m/(s*Pa)) and of frequency (in Hz). Green line represents the estimated acoustic compliance and black dashed line the compliance range for event selections. On the right, histogram of the number of compliance event detections (in color) as a function of logarithm of vertical compliance normalized to wind speed (in 1/Pa) and of frequency (in Hz). Red line represent the selection lower limit for infrasound events. On both panels, red circles present the compliance and normalized compliance values of the suspected infrasounds events described later.

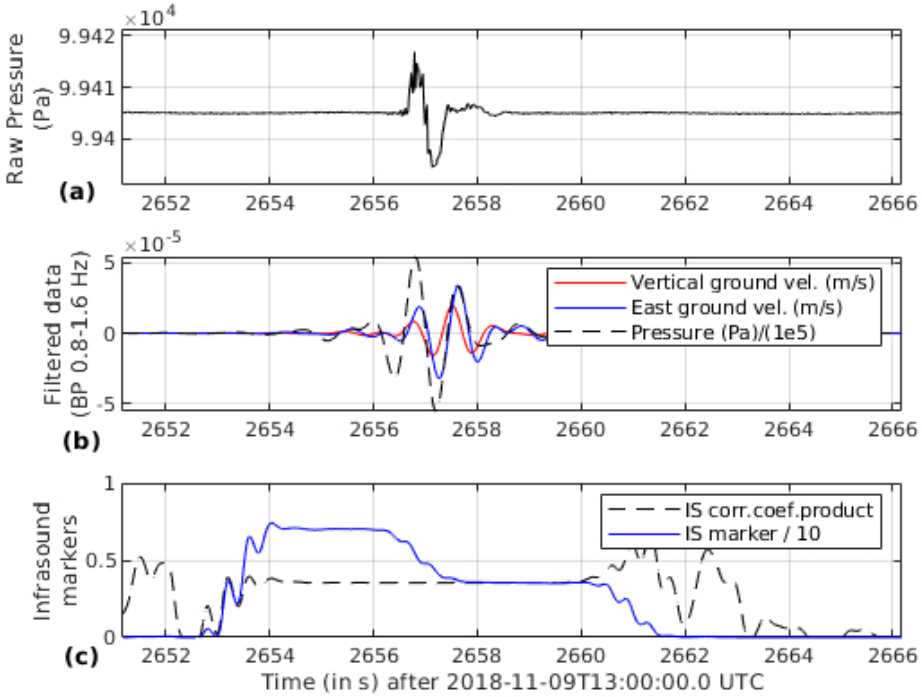

Figure 3. Application of the infrasound marker on the terrestrial data set described by Garcia, Martire, et al. (2020). (a) raw ground pressure records, (b) vertical (red plain line) and horizontal East (blue plain line) ground velocities, as well as scaled ground pressure (black dashed line), band-pass filtered in the 0.8-1.6 Hz range. (c) Product of correlation coefficients in equation (2) (black dashed line) and scaled infrasound marker $I_G(t)$ (blue plain line). Times are given in seconds after 2018-11-09T13:00:00.0 UTC.

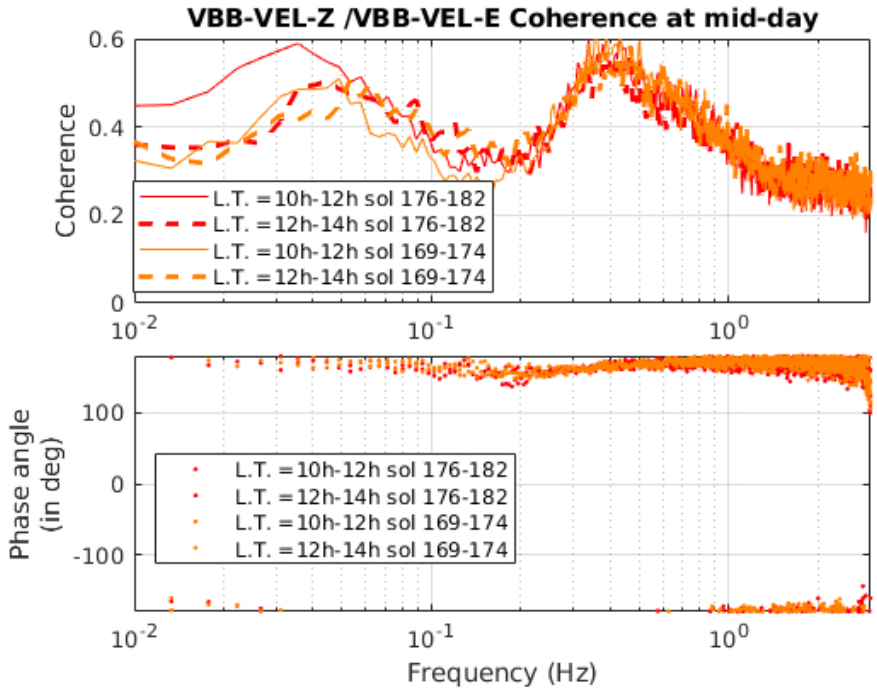

Figure 4. Coherence between vertical and East ground velocity (on top) and associated phase (on the bottom), average over two hours LMST (Local Mean Solar Time), as a function of frequency (in Hz) for different local time ranges around mid-day and different sol ranges.

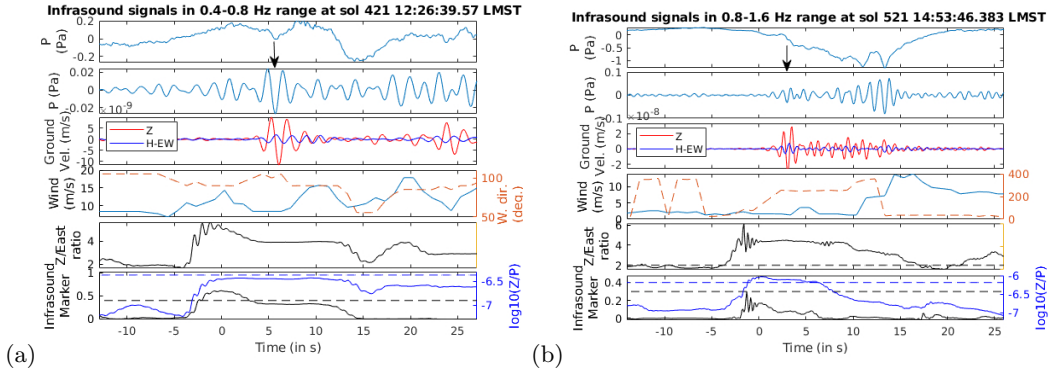

Figure 5. Each panel is presenting an infrasound candidate, (a) in the 0.4-0.8 Hz range, (b) in the 0.8-1.6 Hz range. In Each panel, from top to bottom, Pressure variations (in Pa) above 0.01 Hz, Pressure variations (in Pa) in the considered frequency range, vertical (red line) and East (blue line) ground velocity (in m/s) filtered in the considered frequency range, Wind speed (blue line, in m/s) and direction (brown line, in degrees), Z/East energy ratio, Infrasound marker (black line) and logarithm of measured compliance (blue line, in m/s/Pa) and minimum and expected values for these parameters (horizontal dashed lines). Black arrow indicate the infrasound candidate on the pressure records.

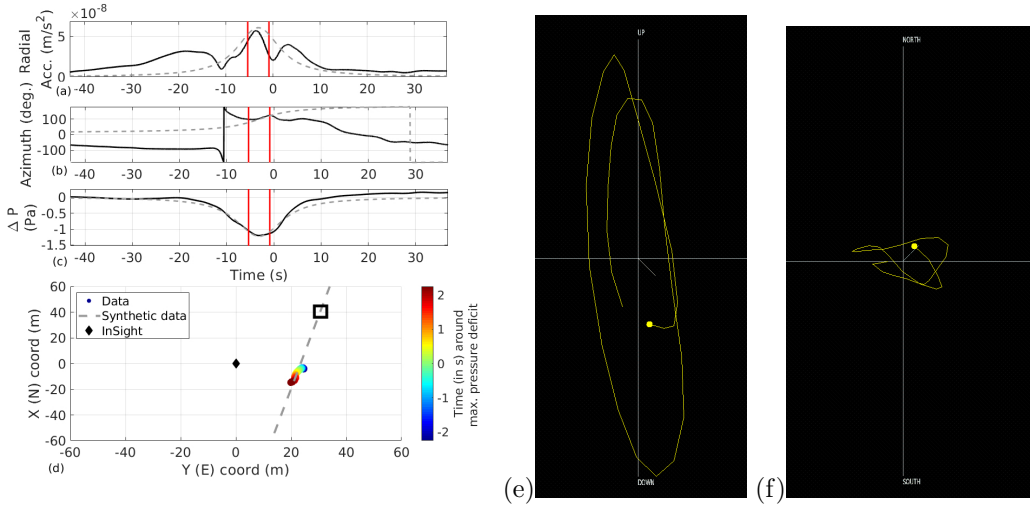

Figure 6. On the left, trajectory reconstruction of the convective vortex immediately following the infrasound candidate on sol 521 (see figure 5.(b)). (a) radial acceleration (in m/s^2) along the estimated azimuth (b), and associated pressure drop (c). Black lines indicate data and dashed grey the values obtained for a best fit synthetic vortex propagating along a linear track. (b) reconstructed trajectory (color filled circles) as a function of time around the pressure minimum (color bar) for a time range corresponding to vertical red lines in panels (a), (b) and (c). Dashed grey indicates the best fit vortex with a linear trajectory. Black square indicates the approximate position of the vortex center at the time of infrasound candidate detection. Panels (e) and (f) provide the polarization of ground velocity records (in the 0.8-1.6 Hz range) during the candidate event, respectively in the Up-East vertical plane seen from South (e), and in the North-East horizontal plane seen from above (f). Yellow dot indicate the start of the signal.

[1]Institut Supérieur de l'Aéronautique et de l'Espace (ISAE-SUPAERO), Université de Toulouse, 10 Ave E. Belin 31400 Toulouse, France
[2]Applied Physics Laboratory, 11100 Johns Hopkins Road, Laurel, Maryland 20723, USA
[3]Laboratoire de Météorologie Dynamique / Institut Pierre-Simon Laplace (LMD/IPSL), Sorbonne Université, Centre National de la Recherche Scientifique (CNRS), École Polytechnique, École Normale Supérieure (ENS), 4 place Jussieu 75005 Paris, France
[4]Institut Universitaire de France (IUF), 1 rue Descartes, 75231 PARIS CEDEX 05, France
[5]Sandia National Laboratories, Albuquerque, NM 87023, USA
[6]Université de Paris, Institut de physique du globe de Paris, CNRS, F-75005 Paris, France
[7]Cornell Center for Astrophysics and Planetary Science, Cornell University, Ithaca, NY, 14853, USA
[8]Jet Propulsion Laboratory, California Institute of Technology, Pasadena, CA 91109, USA
Corresponding author: Raphael F. Garcia raphael.garcia@isae.fr